THE PENNSYLVANIA STATE UNIVERSITY
SCHREYER HONORS COLLEGE

DEPARTMENT OF METOEOROLOGY

AN OBSERVATIONAL AND NUMERICAL STUDY OF INTERNAL GRAVITY WAVES EMBEDDED IN REGIONS OF MOIST SATURATED ASCENT

ROBERT SETZENFAND
Spring 2010

A thesis
submitted in partial fulfillment
of the requirements
for baccalaureate degrees
in Meteorology and Mathematics
with honors in Meteorology

Reviewed and approved* by the following:

John H. E. Clark
Associate Professor of Meteorology
Thesis Supervisor

Johannes Verlinde
Associate Professor of Meteorology
Honors Adviser

* Signatures are on file in the Schreyer Honors College.

ABSTRACT

Sensitivity studies involving a two-dimensional, linear model are used to explain partially the existence of wavelike structures that appear on a visible satellite image. The wavelike structures of interest are present in the overrunning sector of a winter storm. The model resolves mesoscale gravity waves forced by a heating source in an environment with a jet-like background wind. Forecasters may use the results of this study to predict when banded precipitation patterns caused by gravity waves may occur. When the environment includes a surface-based inversion, jet-like background wind, and deep cloud layer, the modeled gravity waves have horizontal wavelengths that are approximately the same as those observed on the visible satellite image.

TABLE OF CONTENTS

LIST OF FIGURES

ACKNOWLEDGEMENTS

I appreciate the specific advice given on this project by John Clark. This thesis could not have been possible without his help. I also appreciate the stellar academic and professional advice that Dennis Thomson provided throughout my time at Penn State. His support aided my pursuit of a Schreyer Honors College Summer Research Grant. The grant allowed me to begin research work during the summer of 2008.

Chapter 1

Introduction

Forecasting weather on small spatial scales and short time periods is a challenging problem. Much is still unknown about mesoscale phenomena and processes in the troposphere. Namely, banded precipitation patterns are examples of mesoscale phenomena lacking understanding. Banded precipitation causes enhanced precipitation rates and the associated precipitation-amount forecasting problems. Some have argued that some banded precipitation patterns could be caused by internal gravity waves (Bosart and Sanders 1986, Bosart and Cussen 1973, Ferguson 1967).

Because these banded patterns exist in the mesoscale, they are sometimes difficult to observe. One observational method is to search for waves in a pressure vs. time plot for surface reporting stations. Another method is to look for wavelike structures on radar reflectivity images, and still another is to find wavelike structures in the cloud deck on visible satellite images.

The environmental make-up at the time of the precipitation is needed to help determine whether gravity waves are the likely cause of the banded precipitation. In a stably stratified environment, parcels displaced upward will initiate gravity waves (Holton 2004). Gravity waves cause fluctuations in the horizontal velocity, vertical velocity, pressure, and buoyancy fields. Given the wavelike patterns of vertical velocity associated with internal gravity waves and the ability to view the resulting cloud patterns on satellite imagery, a case study is appropriate when observing internal gravity waves in regions of saturated ascent. A visible satellite image (Figure 1-1) from 1 February 2008

shows wavelike structures in a cloudy region of the northeastern United States. The region lies north of the surface warm front, according to the surface analyses in Figs. (1-2) and (1-3) from the Hydrometeorological Prediction Center. Classic synoptic meteorology states that the area on the cold side of the warm front is where overrunning is likely to occur, with warm, moist air drawn over a surface-based cool layer. Such a set-up can favor clouds and precipitation to occur on the cold side of the surface warm front. This thesis presents an argument that internal gravity waves are the cause of the wavelike structures seen in the cloud tops on the visible satellite image.

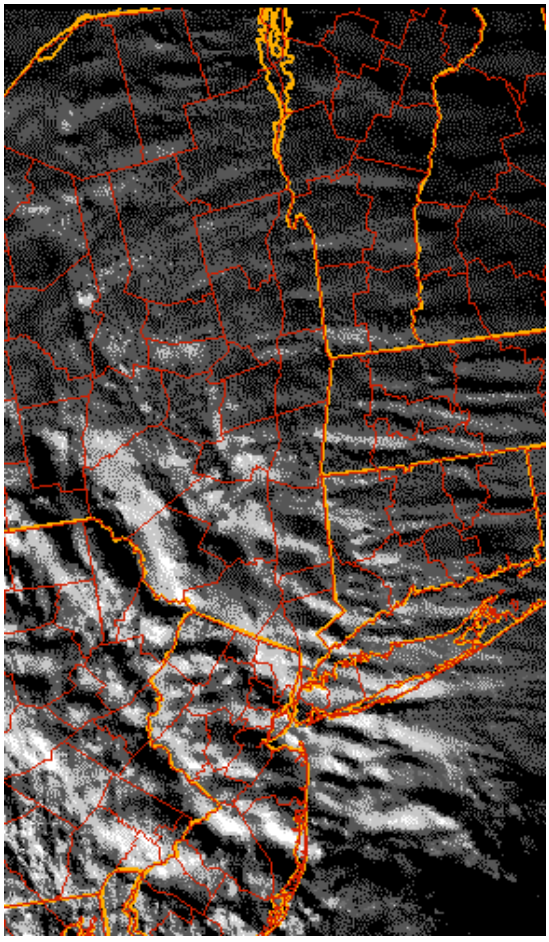

Figure **1-1**. Visible satellite image from 1945 UTC 1 February 2008. Wavelike structures are apparent over New Jersey, eastern New York, Connecticut, western Massachusetts, and Vermont.

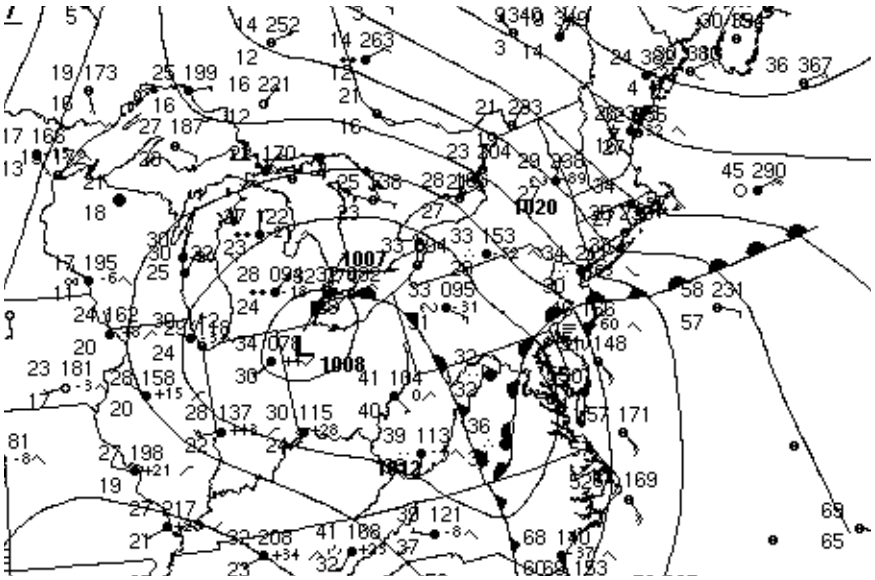

Figure **1-2**. Surface analysis from 1800 UTC 1 February 2008. Source: Hydrometeorological Prediction Center.

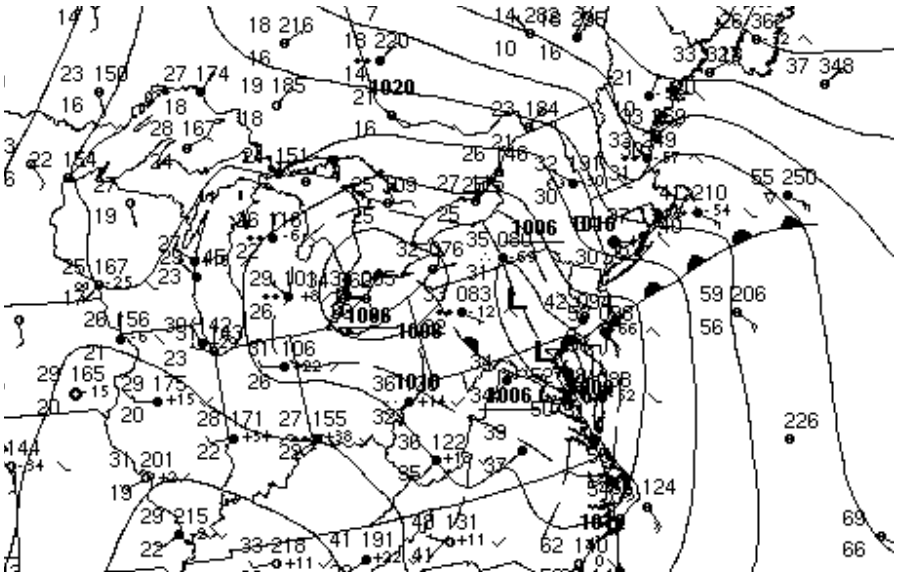

Figure **1-3**. Surface analysis from 2100 UTC 1 February 2008. Source: Hydrometeorological Prediction Center.

Chapter 2

Method

To test the hypothesis that the wavelike structures seen in Fig. (1-1) were caused by internal gravity waves, we used a linear, two-dimensional model of the troposphere and lower stratosphere that resolves gravity waves. This was done so that the response of the waves to changes in the environment could be viewed, and so that the output from a run with background settings similar to the observed environment could be compared with observations.

Experimental procedure

We ran the model with different background conditions to test the sensitivity of the gravity waves. The three background conditions that were altered were the maximum speed of the background wind, an inversion layer with varying depths, and a cloud layer. The first run contained nearly trivial background conditions; no background wind, no cloud layer, and no inversion layer were present. Three additional runs tested the sensitivity of the gravity waves to one background condition per run. The details of what background conditions were included and excluded for each run are in Chapter 3.

The last two sets of runs used background conditions that closely resembled the actual vertical profile of wind and temperature in the Albany, NY to Norfolk, VA corridor around 0000 UTC 2 February 2008, or within a few hours of the wavelike structures appearing on the visible satellite image. Figure (2-1) is a cross-section of the

observed atmosphere that is parallel to the direction of propagation of the wavelike structures seen on the visible satellite image. Two key characteristics of this cross-section are a jet-like background wind with a maximum wind speed of approximately 50 m s^{-1}, and a surface-based inversion. Additionally, Figs. (2-2) and (2-3) are the 0000 UTC 2 February 2008 soundings from Upton, NY and Albany, NY, respectively. Note that the surface-based temperature inversions on both soundings have lapse rates of approximately –4°C/km and they are approximately 1 to 2 km deep. Furthermore, much of the troposphere is saturated. To account for this, we assumed that the cloud base was located at the top of the surface-based inversion.

Model design

The two-dimensional domain of the model extends 850 km horizontally and 25 km vertically. The horizontal domain width was chosen so that (1) it roughly matched the length over which the wavelike structures were observed in the visible satellite image and (2) atmospheric disturbances would not propagate off one side of the vertical plane and return to the opposite side of the vertical plane, which is a consequence of periodic boundary conditions. The outputs of the model are the horizontal and vertical velocity, buoyancy, and pressure perturbations for the lowest 20 km of the domain. Gravity waves were diagnosed by the vertical velocity field in this study.

The model is advanced forward every 15 seconds using a fourth-order Runge-Kutta method. The method works by adding scalar multiples of *time-derivatives* of the horizontal vorticity and buoyancy variables from the previous time step to the horizontal

vorticity and buoyancy variables from the previous time step. We noticed that numerical stability was present with this method, because the Courant-Friedrichs-Lewy number, σ, was about 0.03 for all runs. The Courant-Friedrichs-Lewy condition for numerical stability is

$$\sigma = c\frac{\Delta t}{\Delta x} \le 1,$$

where c is the phase speed of each wave in the Fourier series, Δt is the time step, and Δx is the horizontal grid spacing (Holton 2004).

A sponge layer exists in the uppermost 5 km of the domain to dampen and eliminate vertically propagating gravity waves. It is enacted by multiplying a sponge factor to the time derivatives of horizontal vorticity and buoyancy. The sponge factor $sp(z)$ is defined according to the function

$$sp(z) = \frac{1}{2}\left(1 + \cos\left(\pi\frac{z-20}{5}\right)\right),\ 20\ \text{km} \le z \le 25\ \text{km},$$

where z has units of kilometers. Thus, at z = 20 km, the sponge factor sp is 1, and at z = 25 km, the sponge factor is 0.

The model

- has the tropopause located at 10 km, a typical wintertime tropopause height in the mid-latitudes.
- has a surface-based inversion layer in most runs. The lapse rate in the inversion layer is always –4°C/km. The depth varies from 1 km to 5 km.

- has cloudy regions in most runs. The clouds exist only where vertical velocity is positive within the layer between the top of the inversion and the tropopause. This layer is the cloud layer.
- has a tropospheric lapse rate of 7°C/km outside of any inversion or cloud region and a stratospheric lapse rate of 0°C/km.
- is anelastic and has a background density profile described as $\rho_0 = \rho_{00} e^{-z/H}$, where ρ_{00} is 1.275 kg m^{-3}, a typical value of the surface density, z is height above the surface, and H is 8 km, a typical value of the density scale height.
- neglects the Coriolis force because the Rossby number Ro > 1 for typical values of the horizontal wind speed, Coriolis parameter, and length scale of the observed wavelike phenomena.
- has zero vertical velocity at the lower and upper boundaries. (The streamfunction is zero at the lower and upper boundaries.)
- has periodic boundary conditions on the left and right sides of the domain.
- is semi-spectral: along every line of constant height, each of the three essential variables—mass streamfunction, horizontal vorticity, and buoyancy—is represented as a Fourier series of 51 waves.

Each model run included a heating source within the troposphere that lasted for five minutes. The heating source initiates gravity waves. Such a heating source might appear to be artificial, but the initiation of the gravity waves is not the focus of this study. The spatial distribution of the waves is the primary concern.

The heating was confined to a region 28 km wide by 10 km deep, centered in the middle of the horizontal domain and centered at a height of 6 km. It is projected on all 51 waves at each height within the 10 km-deep region. The heating source in the *x*- and *z*-directions are given by the following formulae in units of K h^{-1}:

$$Q(x) = 5\left(1 + \cos\left(\pi \frac{x - 425}{14.17}\right)\right), \ 410.83 \text{ km} \le x \le 439.17 \text{ km}$$

$$Q(z) = 10 \cos\left(\pi \frac{z - 6}{10}\right), \ 1 \text{ km} \le z \le 11 \text{ km}.$$

Throughout this study, the *x*-direction is simply the horizontal direction in the model domain.

We assumed that the wind had a horizontal component within the model domain defined as

$$u(x,z,t) = U(z) + u'(x,z,t),$$

where $U(z)$ is a jet-like background wind and $u'(x,z,t)$ is the horizontal wind perturbation. The background wind $U(z)$ with units of m s^{-1} is defined as

$$U(z) = \begin{cases} 10, & 0 < z < 1 \text{ km and } 17 \text{ km} < z < 25 \text{ km} \\ 10 + \dfrac{U_{\max}}{2}\left(\cos\left(\dfrac{\pi}{8}(z - 9)\right) + 1\right), & 1 \text{ km} \le z \le 17 \text{ km} \end{cases} \quad (1)$$

where $U_{\max}$ varies from 0 to 40 m s^{-1}, depending on the model run. The vertical component is

$$w(x,z,t) = w'(x,z,t),$$

where w' is the vertical wind perturbation. Motion was governed by the following linearized equations.

$$\frac{\partial u'}{\partial t} + U(z)\frac{\partial u'}{\partial x} + w'\frac{\partial U}{\partial z} = -\frac{1}{\rho_0}\frac{\partial p'}{\partial x} \tag{2}$$

$$\frac{\partial w'}{\partial t} + U(z)\frac{\partial w'}{\partial x} = -\frac{1}{\rho_0}\frac{\partial p'}{\partial z} + b' \tag{3}$$

$$\frac{\partial b'}{\partial t} + U(z)\frac{\partial b'}{\partial x} + N^2(z)w' = Q'(x,z,t) \tag{4}$$

$$\frac{\partial u'}{\partial x} + \frac{1}{\rho_0}\frac{\partial}{\partial z}(\rho_0 w') = 0 \tag{5}$$

Equation (2) is the *x*-momentum equation, (3) is the *z*-momentum equation, (4) is the first law of thermodynamics, and (5) is the continuity equation. Here, p' is the pressure perturbation, b' is the buoyancy perturbation defined as $b' = \frac{\theta - \Theta_0}{\Theta_0} = \frac{\theta'}{\Theta_0}$ (where θ' is the potential temperature perturbation, θ is the potential temperature of a parcel, and Θ_0 is the mean potential temperature on a constant height surface). The Brunt-Väisälä frequency (*N*) is defined as $N = \sqrt{\frac{g}{\Theta_0}\frac{\partial \Theta_0}{\partial z}} = \sqrt{\frac{g}{\overline{T}}(\Gamma_d - \Gamma)}$ with $\overline{T} = 273.15$ K, Q' is the buoyancy source, and ρ_0 is the background density.

If the cloud layer is in use, a nonlinearity arises in (4) because N^2 depends on the sign of the vertical velocity. This is the only nonlinear term in the model. If the vertical velocity is positive, then parcels cool at the moist adiabatic lapse rate of 6°C/km and thus have a different *N* than the surroundings that have zero or negative vertical velocity. Table 2-1 contains the lapse rates for the different layers of the model (inversion, cloudy regions, troposphere outside of the cloudy regions and above the inversion layer, and stratosphere) and the corresponding *N* values.

To find the wind field, we combined (2) and (3) to obtain the horizontal vorticity equation (6):

$$\frac{\partial \eta'}{\partial t} = -U\frac{\partial \eta'}{\partial x} + \frac{\partial^2 U}{\partial z^2}w' + \frac{\partial b'}{\partial x}, \tag{6}$$

where horizontal vorticity η' is defined as

$$\eta' = \frac{\partial w'}{\partial x} - \frac{1}{\rho_0}\frac{\partial}{\partial z}(\rho_0 u') = \frac{1}{\rho_0}\left(\frac{\partial^2 \psi'}{\partial x^2} + \frac{\partial^2 \psi'}{\partial z^2}\right), \tag{7}$$

and ψ' is the mass streamfunction. Every 15 seconds, the model integrates (6) forward in time to find η', and then solves (7) for ψ' using the technique developed by Lindzen and Kuo (1969). Once the ψ' field is known, the horizontal component in the model domain and vertical component of the perturbation wind velocity are found by evaluating (8) and (9).

$$u' = -\frac{1}{\rho_0}\frac{\partial \psi'}{\partial z} \tag{8}$$

$$w' = \frac{1}{\rho_0}\frac{\partial \psi'}{\partial x} \tag{9}$$

Waves found in the vertical velocity field produced by (9) were compared to the observed wavelike structures in the visible satellite image (Fig. 1-1).

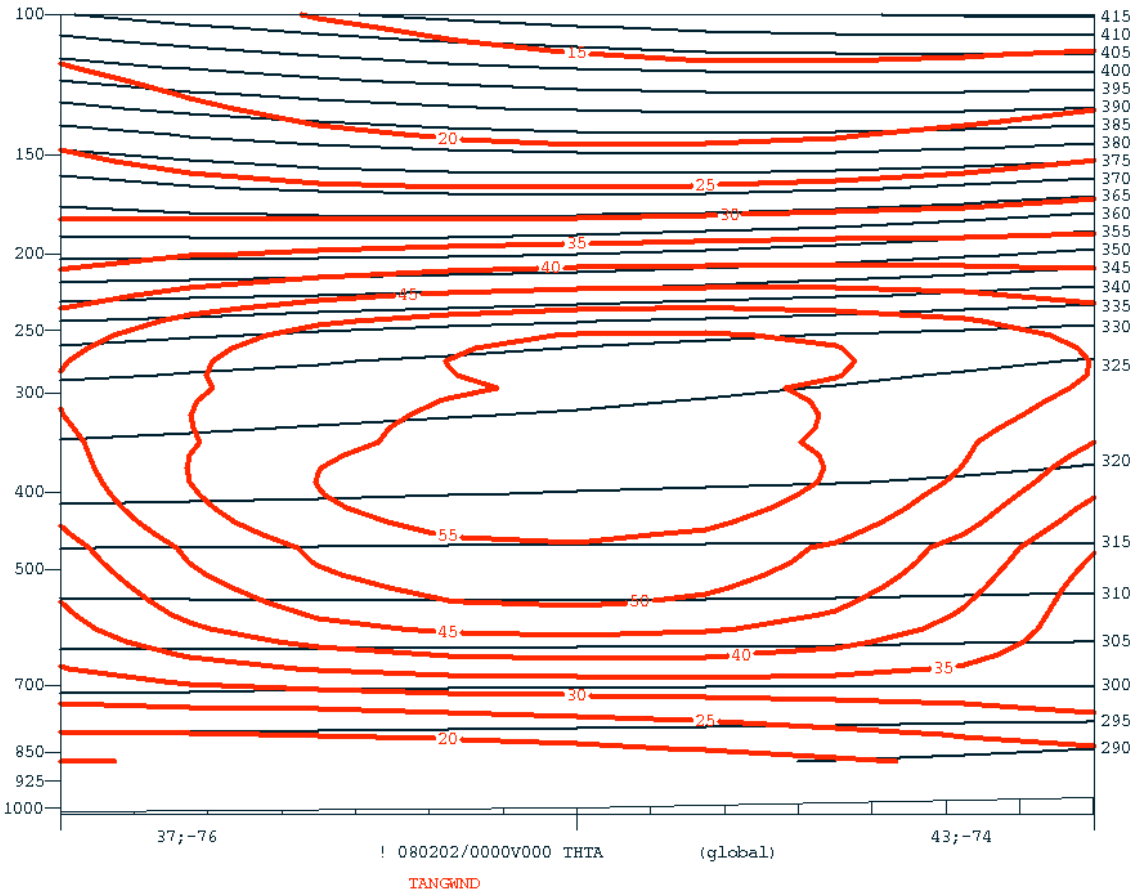

Figure **2-1**. Cross section of potential temperature and horizontal wind speed. Potential temperature is labeled in Kelvin (solid lines) and horizontal wind speed is labeled in m s^{-1} (heavy lines; positive values represent motion from left to right). The cross section runs from 37°N, 76°W to 43°N, 74°W and was generated from observations at 0000 UTC 2 February 2008. Source: MIT Synoptic Laboratory.

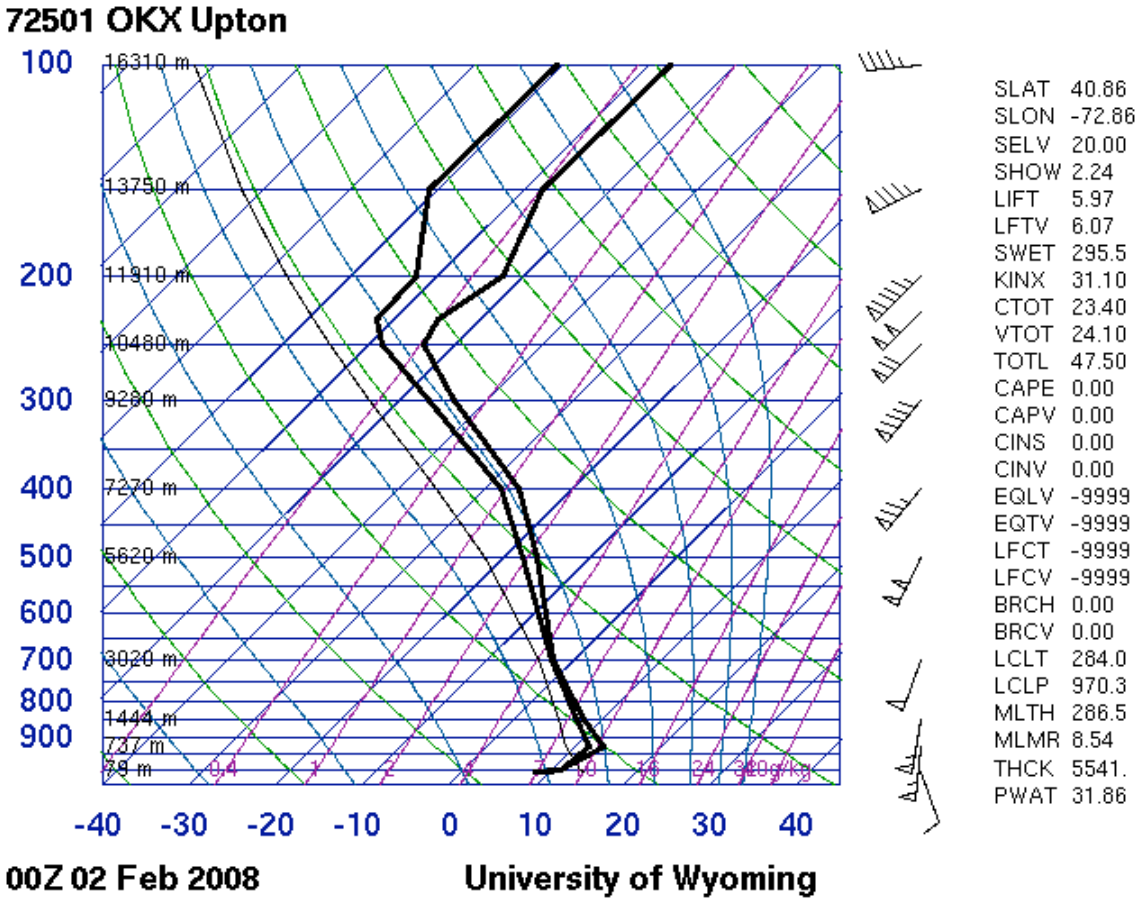

Figure **2-2**. 0000 UTC 2 February 2008 sounding from Upton, NY.

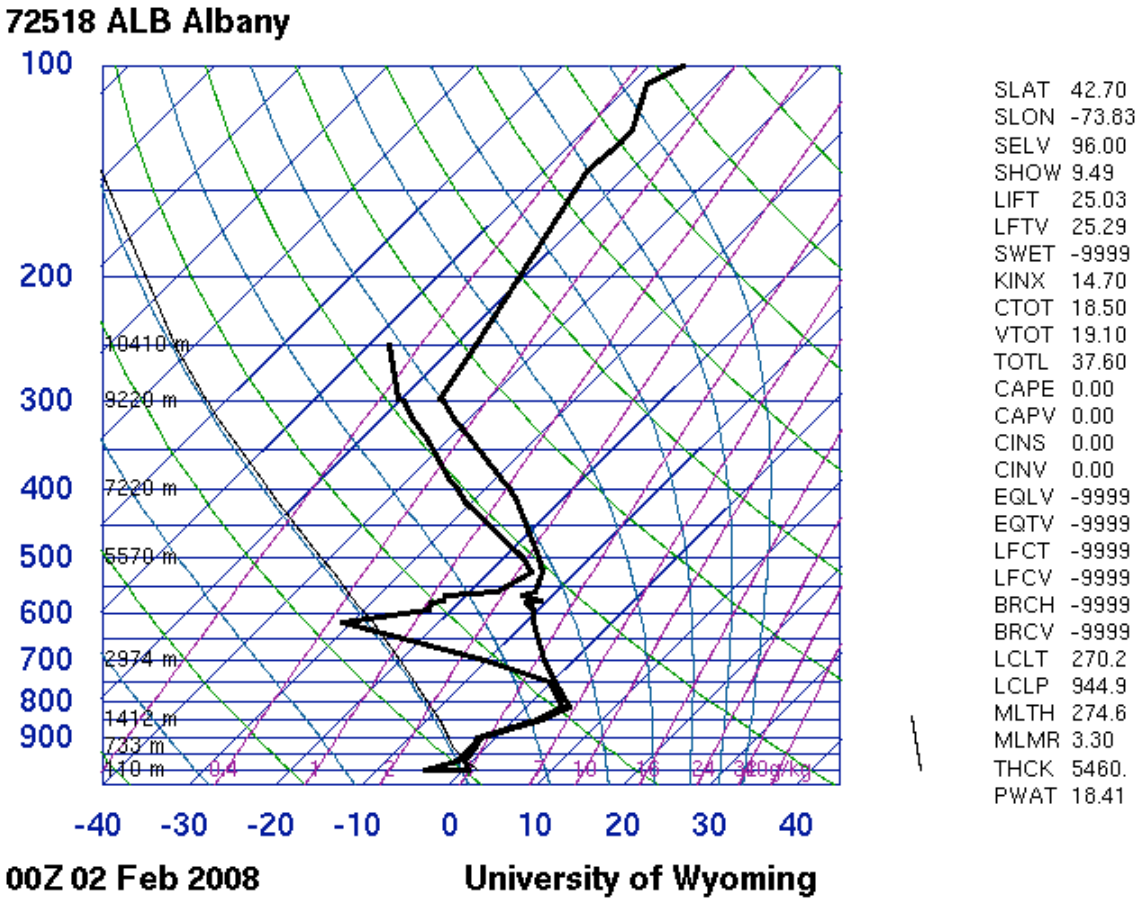

Figure **2-3**. 0000 UTC 2 February 2008 sounding from Albany, NY.

Table **2-1**: Lapse Rates and Corresponding Brunt-Väisälä Frequency Values

Vertical domain	**Lapse rate (°C/km)**	***N*** **(s^{-1})**
Troposphere (top of inversion to tropopause)	7	1.00×10^{-2}
Inversion (surface to cloud base)	–4	2.23×10^{-2}
Cloud (cloud base to tropopause and where $w > 0$)	6	1.17×10^{-2}
Stratosphere (tropopause to 25 km)	0	1.88×10^{-2}

Chapter 3

Results and Discussion

The model was run thirteen times with different background conditions. The background conditions were held constant with time in every run. All runs lasted one hour. The initial run was the trivial run. The trivial run contained no background wind, no cloud layer, and no inversion layer. A heating source initiated gravity waves in the center of the vertical plane. The gravity waves then propagated away from the center. A 170 km-wide portion of the domain where the gravity waves were present is shown in Fig. (3-1). The 170 km-wide cross-section was used for easier viewing purposes; it is simply a portion of the entire 850 km-wide model domain. The figure is the resulting vertical velocity field one hour after the gravity waves were initiated. The distance between two regions of maximum upward vertical velocity along the constant height line $z = 6$ km is about 28.3 km.

The model was then run with one change per run to the background conditions from the trivial, initial run. The second run contained a jet-like background wind profile with a maximum wind speed of 50 m s^{-1} at $z = 9$ km. The cloud and inversion layers were excluded from this run. The resulting vertical velocity field over a 297.5 km-wide domain is Fig. (3-2). No discernible waves are present.

The third run contained no background wind and no cloud layer, but it did include a 2 km-deep surface-based inversion with a lapse rate of –4°C/km. The corresponding Fig. (3-3) reveals a wavelength of roughly 42.5 km at $z = 6$ km. The fourth run contained no background wind and no inversion, but it did contain a cloud layer extending from $z =$

2 km to z = 10 km, the height of the tropopause. Figure (3-4) shows a wavelength of approximately 28.3 km at z = 6 km.

The four runs corresponding to Figs. (3-1) to (3-4) reveal the background conditions to which the waves are most sensitive. In the second, third and fourth runs, only one background condition was turned on while the other two were turned off or set to zero. The waves are most sensitive to the surface-based inversion and the background wind. The inversion case generated a wavelength of 42.5 km, which is greater than the 28.3 km wavelength present in the trivial and cloud layer-only cases. Likewise, there was no discernible wave present in the case in which the background wind was the only background condition being used. No discernible wave is a deviation from the trivial case and its associated 28.3 km wavelength in the vertical velocity field.

Another set of runs tested the sensitivity of the wavelengths to the maximum background wind speed. In Figs. (3-5) to (3-9), a 2 km-deep surface-based inversion with a lapse rate of –4°C/km and a cloud layer extending from the top of the inversion layer to the tropopause were present. The amplitude U_{max} of the jet-like background profile in (1) was the varying environmental parameter. The core of the jet was located at z = 9 km, and it varied from 10 m s^{-1} in Fig. (3-5) to 50 m s^{-1} in Fig. (3-9). The figures reveal that there is some sensitivity to the maximum speed of the background wind. The case of a uniform horizontal background wind with a speed of 10 m s^{-1} [U_{max} = 0 in (1)] yielded the greatest wavelength of roughly 49.6 km. The wavelength then decreased to 45.3 km when a jet-like background wind was introduced with a maximum horizontal wind speed of 20 m s^{-1} at z = 9 km. In Figs. (3-7) and (3-8), the wavelengths decreased further to the 32 to 36 km range as the maximum horizontal wind speed increased to 30

m s^{-1} and 40 m s^{-1} at z = 9 km. Finally, the wavelength increased to approximately 42.5 km when the maximum horizontal wind speed was 50 m s^{-1} at z = 9 km.

The last set of model runs in Figs. (3-10) to (3-13) tested the sensitivity of the wavelengths to the depth of the surface-based inversion. The top of the surface-based inversion also was the base of the cloud deck. Common to each model run within this set were a jet-like background wind profile with a maximum horizontal wind speed of 50 m s^{-1} at 9 km, a cloud layer, and an inversion lapse rate of –4°C/km. The first run included a 1 km-deep surface-based inversion. The resulting vertical velocity field is Fig. (3-10). The vertical velocity field for the run with a 2 km-deep surface-based inversion is Fig. (3-9). Figures (3-11) to (3-13) reveal the vertical velocity fields for surface-based inversions that were 3 to 5 km deep. The wavelengths seem to be less sensitive to the inversion depth than they were to the maximum background wind speed. The wavelengths ranged from 42.5 km to 45.3 km as the inversion depth varied from 1 km to 5 km.

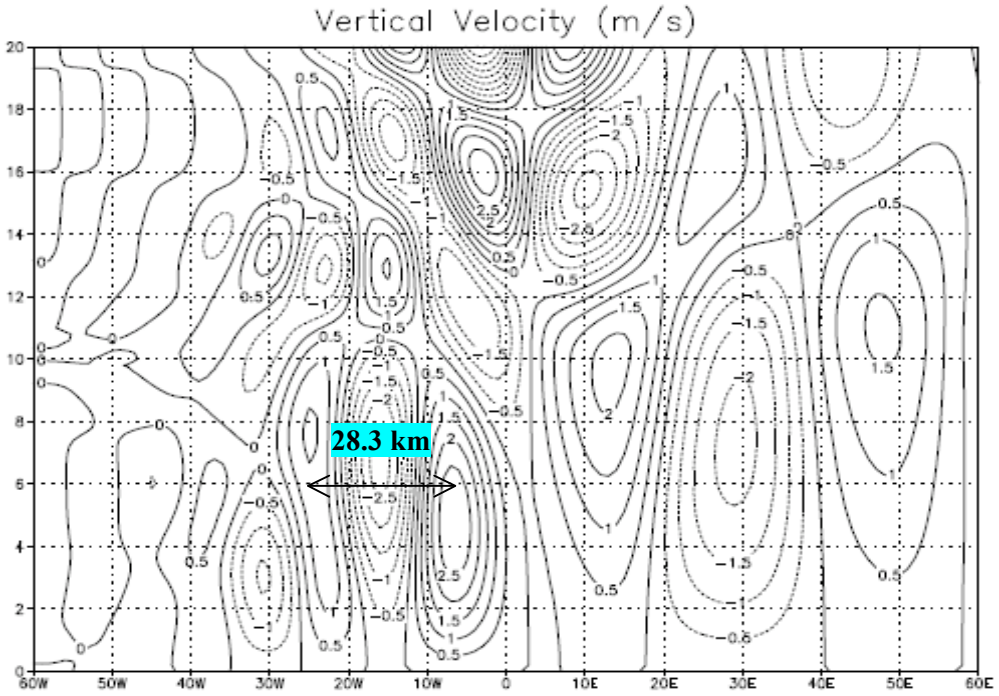

Figure **3-1**: Modeled vertical velocity field with no background wind, no cloud, and no inversion. The horizontal domain is 170 km wide.

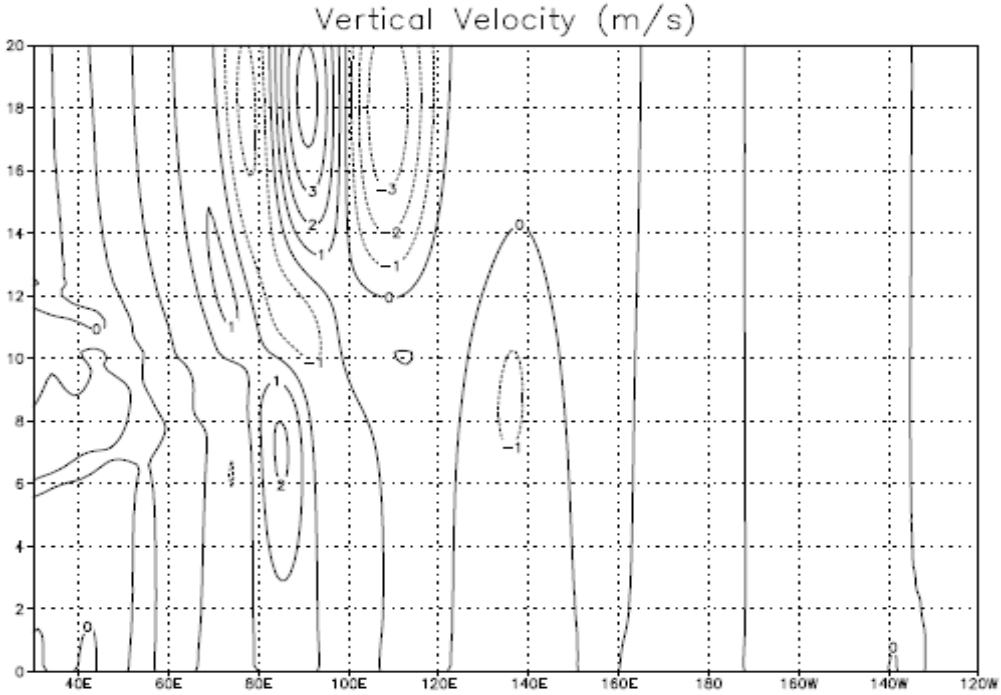

Figure **3-2**: Modeled vertical velocity field with a jet-like background wind. The background wind speed varies from 10 m s^{-1} below 1 km and above 17 km to its maximum speed of 50 m s^{-1} at 9 km. Inversion and cloud layers have been excluded from this run. The horizontal domain is 297.5 km wide.

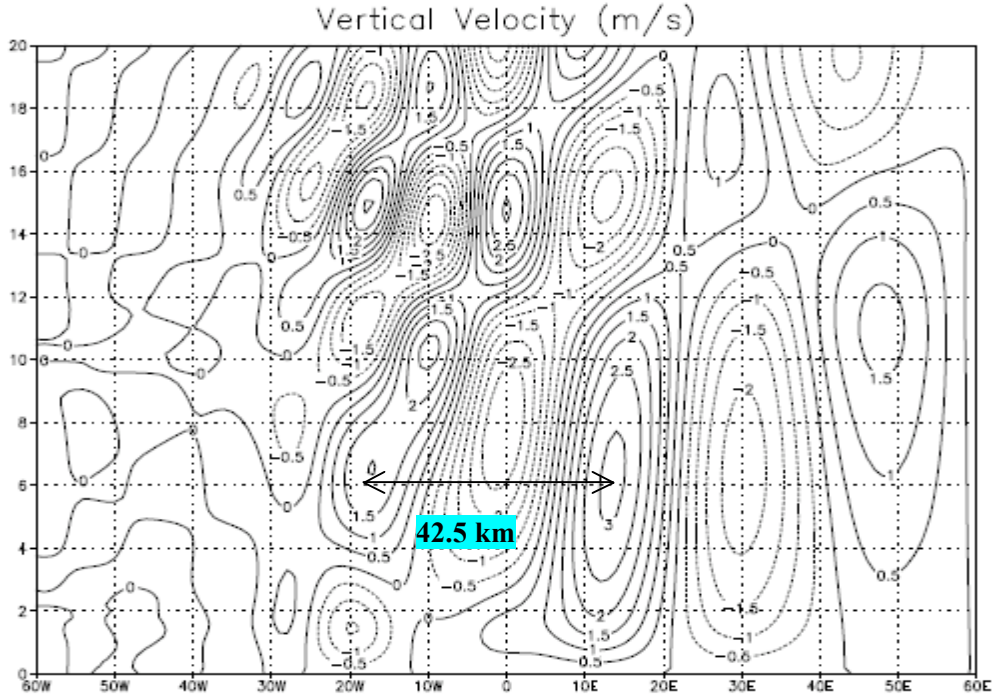

Figure **3-3**: Modeled vertical velocity field with a surface-based, 2 km-deep inversion. The cloud layer and background wind have been omitted. The horizontal domain is 170 km wide.

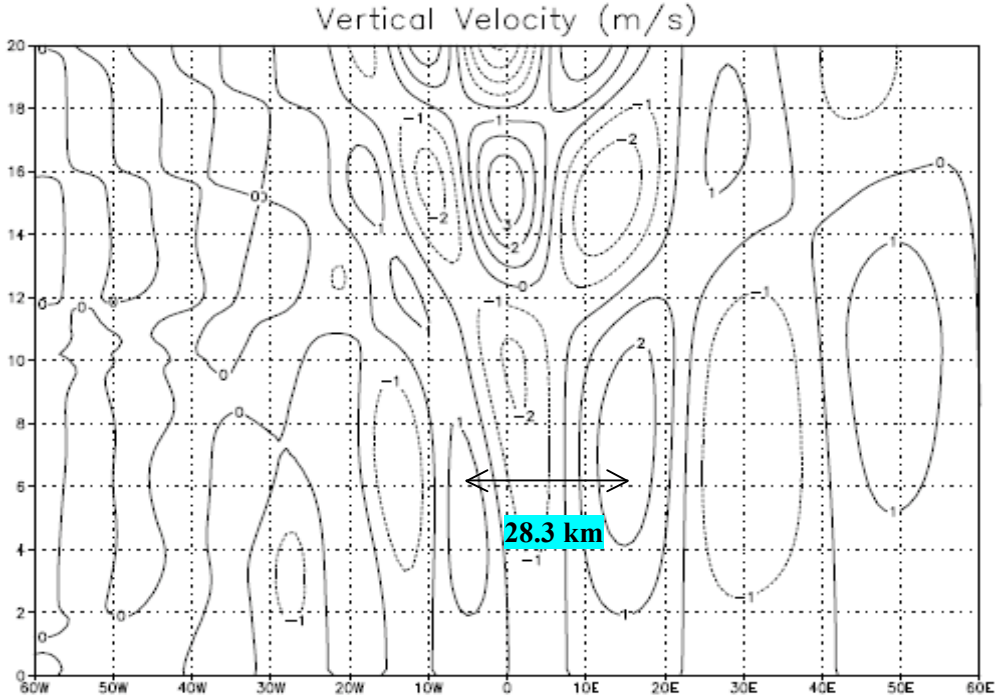

Figure **3-4**: Modeled vertical velocity field with a cloud layer from 2 km above the surface to the tropopause, at 10 km. The inversion layer and background wind have been omitted. The horizontal domain is 170 km wide.

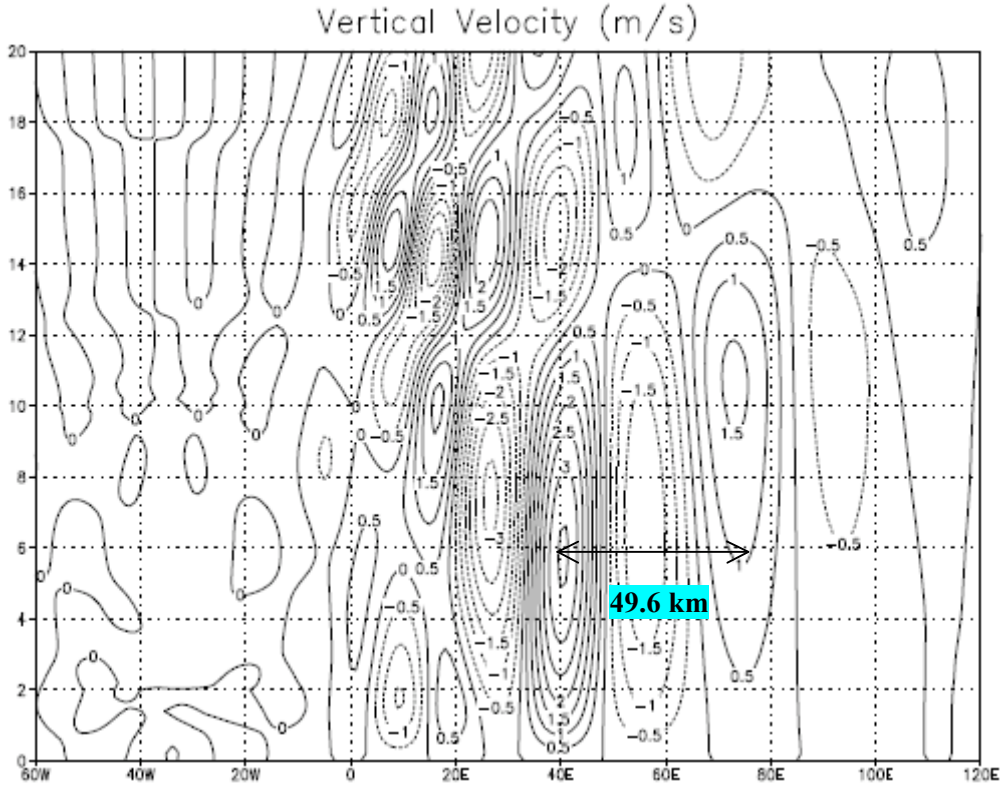

Figure **3-5**: Modeled vertical velocity field with a surface-based, 2 km-deep inversion; cloud layer; and a 10 m s^{-1} background wind that is independent of height. The horizontal domain is 255 km wide.

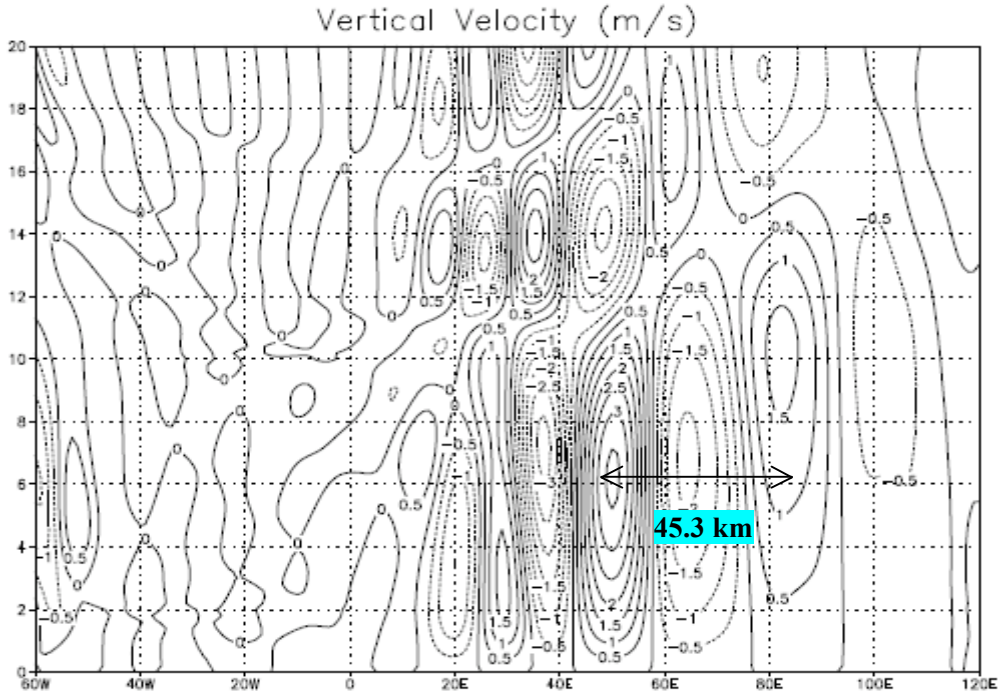

Figure **3-6**: Modeled vertical velocity field with a surface-based, 2 km-deep inversion; cloud layer; and a jet-like background wind (maximum speed 20 m s^{-1}). The background wind speed varies from 10 m s^{-1} below 1 km and above 17 km to its maximum speed at 9 km. The horizontal domain is 255 km wide.

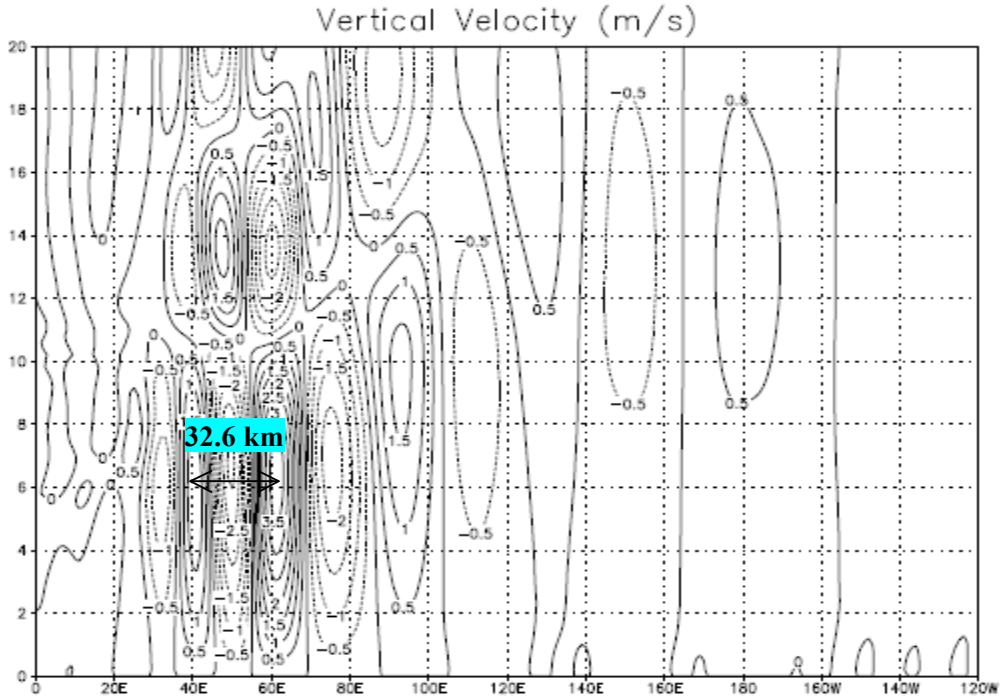

Figure **3-7**: Modeled vertical velocity field with a surface-based, 2 km-deep inversion; cloud layer; and a jet-like background wind (maximum speed 30 m s^{-1}). The background wind speed varies from 10 m s^{-1} below 1 km and above 17 km to its maximum speed at 9 km. The horizontal domain is 340 km wide.

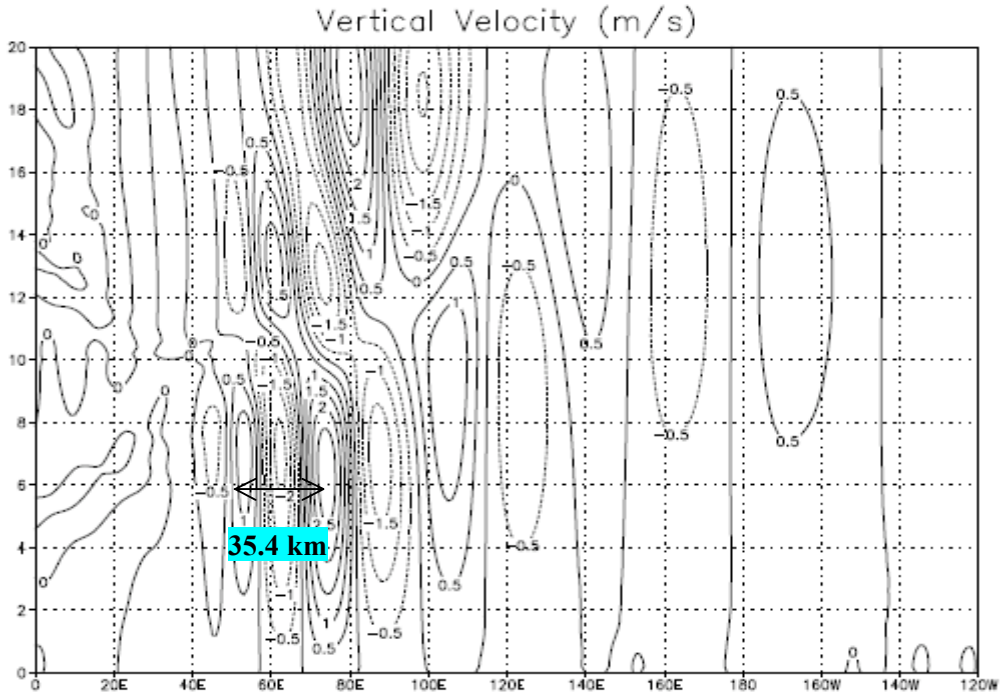

Figure **3-8**: Modeled vertical velocity field with a surface-based, 2 km-deep inversion; cloud layer; and a jet-like background wind (maximum speed 40 m s^{-1}). The background wind speed varies from 10 m s^{-1} below 1 km and above 17 km to its maximum speed at 9 km. The horizontal domain is 340 km wide.

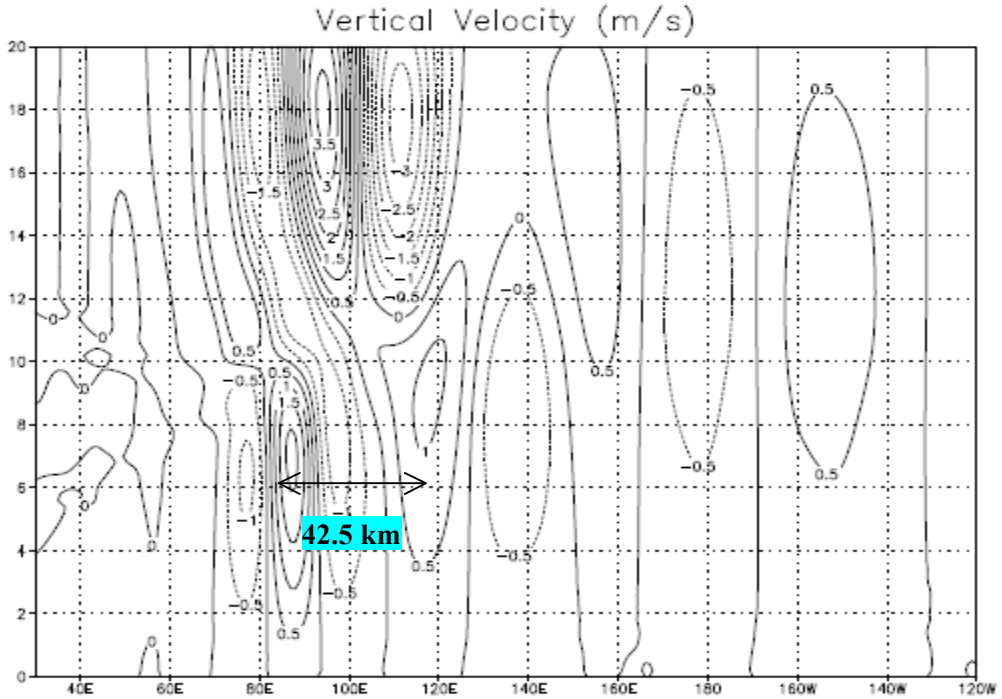

Figure **3-9**: Modeled vertical velocity field with a surface-based, 2 km-deep inversion; cloud layer; and a jet-like background wind (maximum speed 50 m s^{-1}). The background wind speed varies from 10 m s^{-1} below 1 km and above 17 km to its maximum speed at 9 km. The horizontal domain is 297.5 km wide.

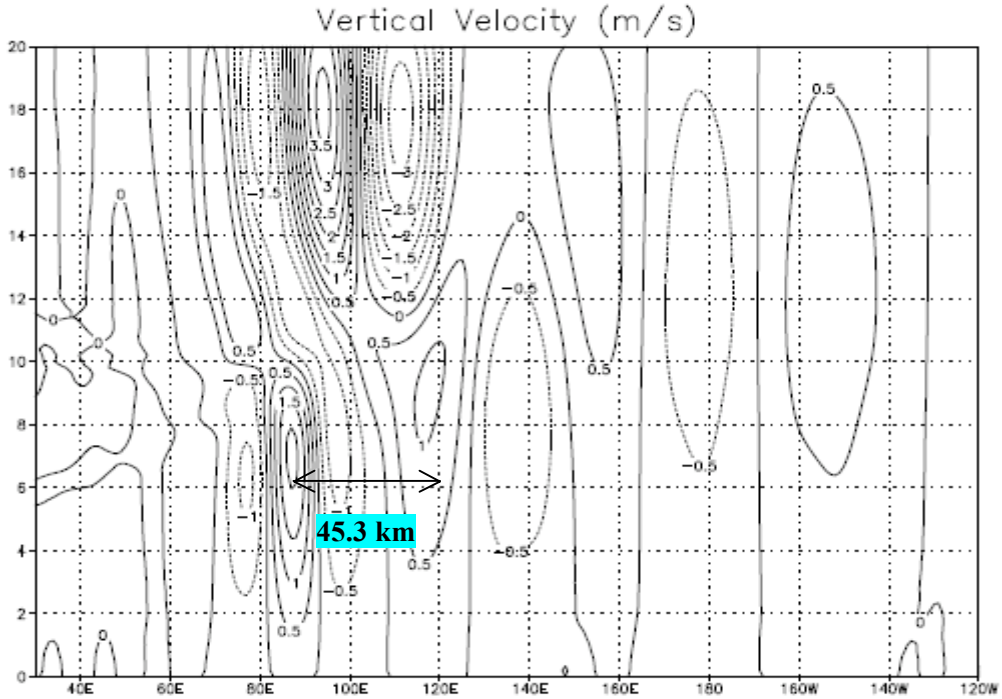

Figure **3-10**: Modeled vertical velocity field with a surface-based, 1 km-deep inversion; cloud layer; and a jet-like background wind (maximum speed 50 m s^{-1}). The background wind speed varies from 10 m s^{-1} below 1 km and above 17 km to its maximum speed at 9 km. The horizontal domain is 297.5 km wide.

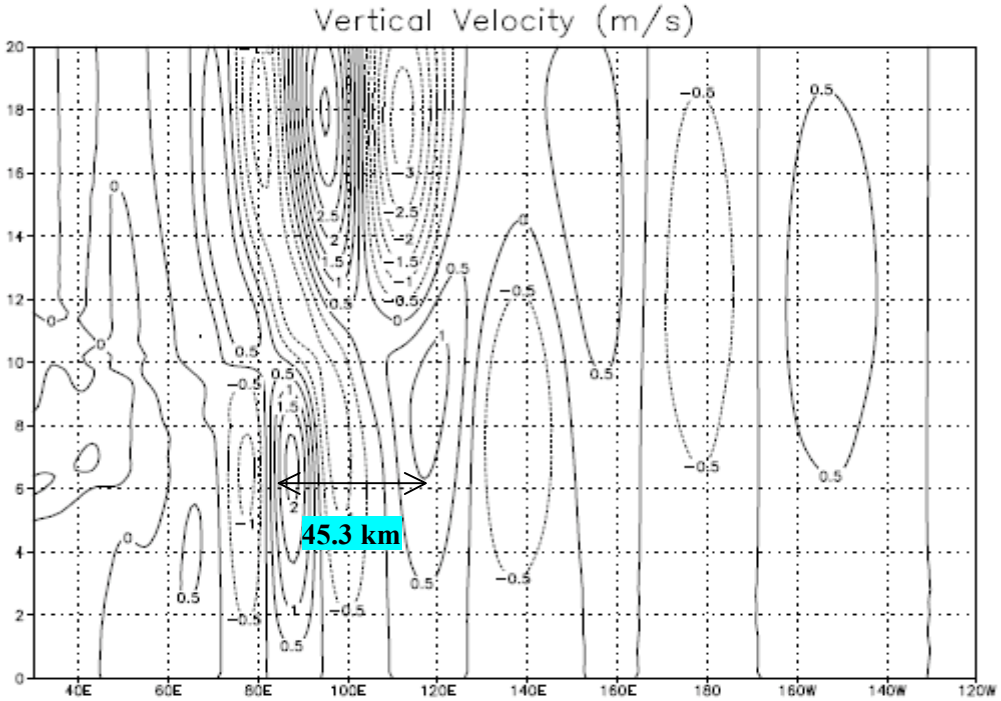

Figure **3-11**: Modeled vertical velocity field with a surface-based, 3 km-deep inversion; cloud layer; and a jet-like background wind (maximum speed 50 m s^{-1}). The background wind speed varies from 10 m s^{-1} below 1 km and above 17 km to its maximum speed at 9 km. The horizontal domain is 297.5 km wide.

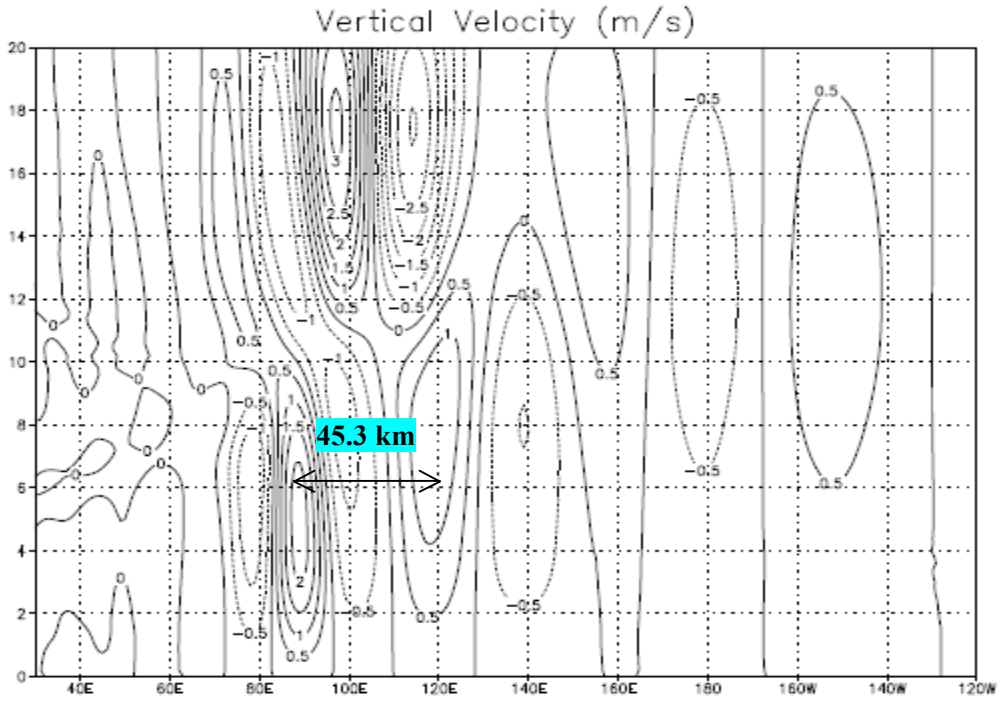

Figure **3-12**: Modeled vertical velocity field with a surface-based, 4 km-deep inversion; cloud layer; and a jet-like background wind (maximum speed 50 m s^{-1}). The background wind speed varies from 10 m s^{-1} below 1 km and above 17 km to its maximum speed at 9 km. The horizontal domain is 297.5 km wide.

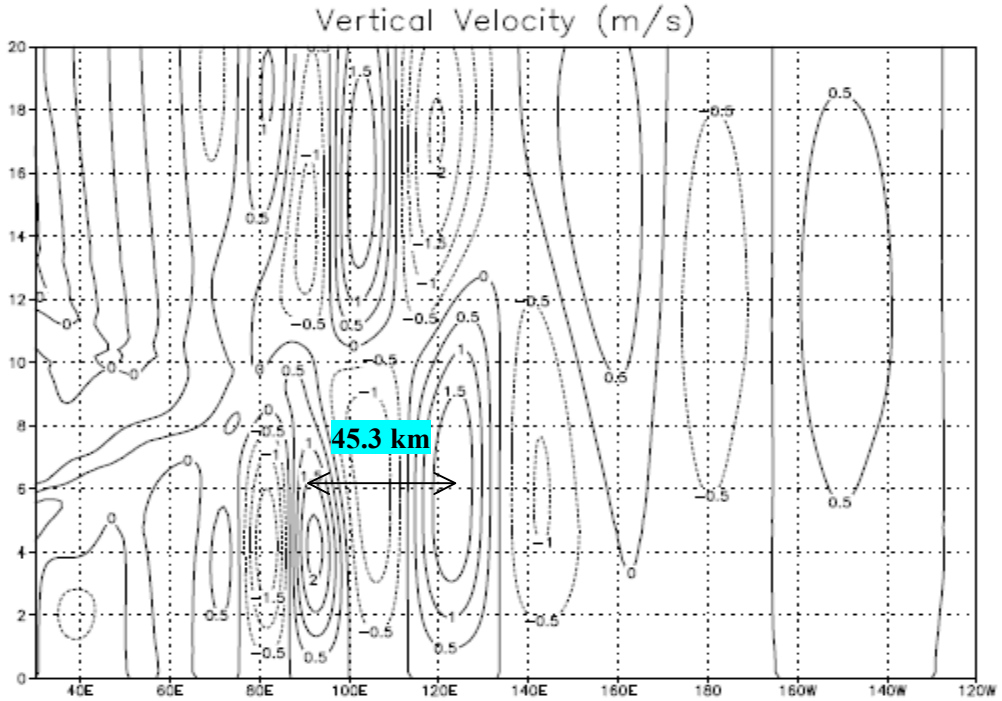

Figure **3-13**: Modeled vertical velocity field with a surface-based, 5 km-deep inversion; cloud layer; and a jet-like background wind (maximum speed 50 m s^{-1}). The background wind speed varies from 10 m s^{-1} below 1 km and above 17 km to its maximum speed at 9 km. The horizontal domain is 297.5 km wide.

Chapter 4

Conclusion

The horizontal wavelengths in the vertical velocity field were most sensitive to the presence of a surface-based inversion and the maximum speed of the jet-like background wind. The inclusion of only a surface-based inversion generated a 14 km increase in the wavelength from the trivial state. The wavelengths were not as sensitive to the depth of the inversion. The inclusion of only a jet-like background wind with a maximum speed of 50 m s^{-1} did not generate any discernible waves. Once the inversion and cloud layers were included, waves did appear with nonzero values of U. The different values of U_{max} generated wavelengths that ranged roughly from 33 km to 50 km. The wavelengths were not sensitive to the inclusion of a cloud layer.

The results support the hypothesis that internal gravity waves likely are the cause of the wavelike structures seen in the visible satellite image (Figure 1-1). The model was run with background conditions that were similar to those observed along a line perpendicular to the phase fronts of the wavelike structures on the satellite image. The wavelengths that were observed in the cloud deck on the satellite image ranged from 29 km to 38 km. Model runs of one hour produced wavelike structures in the vertical velocity field that had horizontal wavelengths close to those observed on the visible satellite image. Forecasters can be alert for gravity waves in the overrunning sector of winter storms given the tendency for the sector to contain a large area of moisture, a surface-based inversion, and a jet-like background wind.

Future work may explain the duration of the waves, as the waves persisted for a few hours on 1 February 2008. Ducting is a possible cause for the long duration, as discussed by Lindzen and Tung (1976).

References

Bosart, L. F., and J. P. Cussen, 1973: Gravity Wave Phenomena Accompanying East Coast Cyclogenesis. *Mon. Wea. Rev.*, **101**, 446–454.

Bosart, L. F., and F. Sanders, 1986: Mesoscale Structure in the Megalopolitan Snowstorm of 11-12 February 1983. Part III: A Large Amplitude Gravity Wave. *J. Atmos. Sci.*, **43**, 924–939.

Ferugson, H. L., 1967: Mathematical and Synoptic Aspects of a Small-Scale Wave Disturbance Over the Lower Great Lakes Area. *J. Appl. Meteor.*, **6**, 523–529.

Holton, J. R. 2004: An Introduction to Dynamic Meteorology. Elsevier Academic Press, New York, NY, 535 pp.

Lindzen, R. S., and H. L. Kuo, 1969: A Reliable Method for the Numerical Integration of a Large Class of Ordinary and Partial Differential Equations. *Mon. Wea. Rev.*, **97**, 732–734.

Lindzen, R. S., and K. K. Tung, 1976: Banded Convective Activity and Ducted Gravity Waves. *Mon. Wea. Rev.*, **104,** 1602–1617.

ACADEMIC VITA of Robert M. Setzenfand

Robert M. Setzenfand
303 Laurel Hill Road
Allison Park, PA 15101
robert.setzenfand@gmail.com

Education: Bachelor of Science Degrees in Meteorology and Mathematics,
Penn State University, Spring 2010
Honors in Meteorology
Thesis Title: An Observational and Numerical Study of Internal Gravity Waves Embedded in Regions of Moist Saturated Ascent
Thesis Supervisor: John H. E. Clark

Related Experience:
Internship with the Office of Hydrologic Development (a part of the National Oceanic and Atmospheric Administration)
Supervisor: Mr. David Kitzmiller
Summer 2009

Awards:
John A. Dutton Award in Atmospheric Dynamics
President's Freshman Award
Dean's List
Phi Beta Kappa
Chi Epsilon Pi

Presentations/Activities:
Presented internship project results at the 2009 National Oceanic and Atmospheric Administration Science and Education Symposium
Tutored students in mathematics at State College Area High School